Structural refinement and crystal chemistry of Mn-doped spinel: A case for tetrahedrally coordinated Mn³⁺ in an oxygen-based structure

FERDINANDO BOSI,[1,*] ULF HÅLENIUS,[1] GIOVANNI B. ANDREOZZI,[2] HENRIK SKOGBY,[1]
AND SERGIO LUCCHESI[2]

[1]Department of Mineralogy, Swedish Museum of Natural History, Box 50007, 10405 Stockholm, Sweden
[2]Dipartimento di Scienze della Terra, Università di Roma "La Sapienza," P.le A.Moro 5, 00185 Roma, Italy

ABSTRACT

Spinel single crystals of four compositions along the $MgAl_2O_4$–$MgMn_2O_4$ join, with Mn^{3+} up to 0.25 apfu, were synthesized by use of a flux-growth method. The crystals were analyzed by electron microprobe, X-ray single-crystal diffraction, and optical absorption spectroscopy. Results revealed that Mg contents vary from 0.90 to 0.99 apfu, $Mn^{2+} \leq 0.11$ apfu, Mn^{3+} varies from zero to 0.25 apfu, and Al-contents from 1.75 to 1.99 apfu. The unit-cell parameter increases linearly from 8.0883(3) to 8.1413(4) Å with increasing Mn^{3+} content. The crystals show moderately disordered cation distributions, with $i = 0.23(1)$, and different distribution trends have been observed: the Mg content is constant at the T site and is replaced by Mn^{2+} at the M-site; Al decreases while Mn^{3+} increases in T- and M-sites. Mn^{3+} shows a preference for the T site, and a specific bond distance was refined, $^{IV}Mn^{3+}$-O = 1.88(1) Å. Unpolarized room-temperature single-crystal spectra reveal two relatively broad absorption features at ca. 23 000 and 10 800 cm^{-1}, which are assigned to spin-allowed d-d transitions in Mn^{3+} located at octahedral and tetrahedral sites, respectively. The bond valence approach shows that the bonds are strained in the tetrahedron indicating underbonding in T, whereas the bonds are unstrained in the octahedron. To reduce the M-M repulsion, the steric effect is driven by the movement of the oxygen atoms, which improves the shielding effect around the M-site, thus increasing the distortion of the structure relative to the CCP. As a result the tetrahedron undergoes an isotropic expansion, which constrains the structure to incorporate larger cations such as Mn^{3+} rather than smaller cations like Al at the T-site. This behavior, which is in disagreement with predictions based on crystal field energy considerations, illustrates the greater importance of steric factors on the cation distribution in spinels.

Keywords: Chemical analysis (mineral), spinel, crystal structure, optical spectroscopy, Mn^{3+} in spinel, order-disorder, XRD data

INTRODUCTION

Multiple oxides with spinel type structure may be described by the $^{IV}(A_{1-i}B_i)^{VI}(B_{2-i}A_i)O_4$ structural formula, where A and B are cations with variable valence (usually, A^{2+} and B^{3+}) and i is the inversion parameter. Normal spinels are those with $i = 0$, inverse spinels have $i = 1$. The structure is generally described as a Cubic Close Packed (CCP) array of anions, with A and B cations distributed in one-eighth of all tetrahedral (T) and half of all octahedral (M) sites. The unit cell is face-centered cubic ($Fd\overline{3}m$) and it contains 32 anions. The cations are fixed at special positions 8a (T) and 16d (M). Anions also occupy a special position, 32e, but with a variable fractional coordinate (u,u,u). With the origin at $\overline{3}m$, the parameter u ranges from 0.24 to 0.27. The u value is an indicator of the regularity of the CCP. For the ideal close packed structure, $u = 0.25$, the anions form regular tetrahedral (8a point symmetry $\overline{4}3m$) and octahedral interstices (16d point symmetry $m3m$). A distortion of the CCP arises when $u \neq 0.25$. If u increases, oxygen is displaced along the [111] direction, causing an expansion of the tetrahedron at the expense of the octahedron. As the positions of cations A and B are fixed, the oxygen array expands (or contracts) around them. In this way, the octahedron

undergoes angular distortion and its symmetry degenerates to $\overline{3}m$ (trigonally distorted octahedra), whereas the tetrahedron remains regular. The fractional coordinate is thus closely related to the distortion of the CCP, and sometimes an increase in u is required to reduce M-M repulsion and thereby ensure energetic stabilization of the structure (Lavina et al. 2003).

The structure is rigid, with only two variable parameters, u and a, which describe all geometrical relations in the structure (Hill et al. 1979). When the T-site population is constant, u is inversely proportional to the M-O distance, while when the M-site population is constant, u is directly proportional to the T-O distance. The isolated TO_4 tetrahedron is surrounded by 12 MO_6 octahedra. Structural interaction between T and M are known to result in isotropic lengthening of T-O. This phenomenon is due to M-site occupancies (e.g., Fe^{3+} and V^{3+}) and/or T-site vacancy (Lavina et al. 2002, 2003; Bosi et al. 2004).

The presence of cations subjected to Jahn-Teller distortion, such as Mn^{3+}, in the M-octahedron lowers its point symmetry to 2/m (tetragonal bipyramid) by formation of two long (M-O_L) and four short (M-O_S) bonds. This tetragonal elongation will effectively produce large-scale effects only when the critical $^{VI}Mn^{3+}$ concentration and temperature is reached (Golikov et al. 1989). The overall effect is a transition from cubic ($Fd\overline{3}m$) spinel

---

* E-mail: ferdinando.bosi@nrm.se

symmetry to tetragonal ($I4_1/amd$) symmetry.

Literature on the structural details of spinels along the join $MgAl_2O_4$–$MgMn_2O_4$ is scarce. Keer et al. (1974) investigated physical and structural properties of this binary system, but their structural study was restricted to cell parameter determinations, which reflected a transition from cubic to tetragonal symmetry at a critical concentration of 87 mol% $MgMn_2O_4$. This value is high compared to the system $MnFe_2O_4$–$MnMn_2O_4$, in which the corresponding transition takes place at a concentration of ca. 35 mol% $MnMn_2O_4$ (Matsubara et al. 1979). This difference is explained by the Mn^{3+}-occupancy of T-sites in $MgAl_2O_4$–$MgMn_2O_4$ solid-solution spinels (Keer et al. 1974), which reduces the formation of Jahn-Teller distorted octahedra. A disordered Mn^{3+}-distribution is in fact observed even at low temperatures in the $MgMn_2O_4$ end-member (Radhakrishnan and Biswas 1975, 1976; Malavasi et al. 2002, 2005). According to these authors, the inversion changes with the temperature from 22 to 40%.

In this work, we have attempted to synthesize spinel single crystals along the first part of the join $MgAl_2O_4$–$MgMn_2O_4$, well below the phase transition, with the aim of investigating the Mn site partitioning and its effects on structural parameters and optical properties.

EXPERIMENTAL METHODS

Synthesis

Spinel single crystals samples of four different nominal compositions along the $MgAl_2O_4$–$MgMn_2O_4$ solid-solution join were synthesized by use of a flux-growth method. Spinel components were weighed out in pre-dried oxide form (analytical grade) in proportions to the desired compositions, with a 17% deficiency for Al_2O_3 to compensate for the refractive nature of this compound. The oxides were mixed with $Na_2B_4O_7$ acting as flux compound, using flux/oxide ratios ranging from 1.3 to 1.5, and were homogenized under acetone in an agate mortar. Approximately 7 g of these mixtures were placed in 12 mL platinum crucibles, covered by lids, and placed in a muffle furnace under ambient atmosphere conditions. In the thermal runs, the temperature was first increased to 1200 °C and then kept constant for 24 h to allow for complete dissolution of the oxides and melt homogenization. Subsequently, the temperature was decreased by 4 °C/h to 800 °C, followed by faster cooling down to ambient temperature.

The synthesis products consisted of spinel and elongated borate crystals dispersed in sodiumborate glass. The borate crystals and glass were dissolved in a warm diluted HCl solution.

Single-crystal structural refinement

One single crystal (100–200 μm) from each synthesis run was handpicked and prepared for X-ray data collection. The crystals were mounted on a Siemens P4 automated four-circle, single-crystal diffractometer. Details of the data collection are summarized in Table 1.

For collection of diffraction intensity data, one-eighth of the reciprocal space was examined with the ω scan method at a fixed scan range. The scan speed was variable, depending on reflection intensity, as estimated through pre-scans. The background was measured with a stationary counter and crystal at the beginning and end of each scan, in both cases for half the scan time. Three standard reflections were monitored every 47 measurements. Further details of the experimental conditions can be found in Lucchesi et al. (1997).

The SHELXTL-PC program package was used for reduction of X-ray diffraction data. Intensities were corrected for polarization and Lorentz effects. Absorption corrections were accomplished with a semi-empirical method (North et al. 1968). Only reflections with $I > 2\sigma(I)$ were used in the refinements. No significant deviations from $Fd\bar{3}m$ symmetry were noted. Appearance of forbidden space-group reflections such as 200 was attributed, on the basis of ψ-scan checks, to double reflection (Tokonami and Horiuchi 1980). Variable parameters during the structural refinements were scale factor, oxygen coordinate, mean atomic number (m.a.n.) of T and M sites, displacement parameters, and isotropic secondary extinction coefficients (Table 2). The starting oxygen coordinate proposed by Lucchesi et al. (1997), setting the origin at $\bar{3}m$, was used.

No chemical constraints were applied during the refinements. Fully ionized scattering curves for all elements except oxygen (80% ionized) were applied as these resulted, as observed by Della Giusta et al. (1996), in the best conventional agreement factors over all sinθ/λ intervals and the best coherence between observed and calculated F (222). Three isotropic, full-matrix, refinement cycles were followed by anisotropic cycles until convergence was attained (Table 2).

Electron microprobe analysis

The crystals used for X-ray data collection were mounted on a glass slide and polished for electron microprobe analysis (WDS method) with a Cameca SX50 instrument operating at an accelerating potential of 15 kV and a sample current of 15 nA, at IGG-CNR, Padova. Synthetic phases of $MgCr_2O_4$, $MnTiO_3$, and Al_2O_3 were used as standards, and a synthetic $MgAl_2O_4$ spinel served as a reference. Each element determination was accepted after checking that the line intensity of the analyzed standards before and after each measurement was within 1.00 ± 0.01. For raw data reduction, the PAP computer program was applied (Pouchou and Pichoir 1984). Mn^{2+} and Mn^{3+} were calculated from the measured Mn_{tot} concentration on the basis of the spinel formula with 3 cations for 4 O atoms. The results, which are summarized in Table 3, represent mean values of a minimum of 30 spot analyses per analyzed crystal.

Cation distribution determination

The intracrystalline cation distribution was calculated by an optimization program applying a minimization function, $F(X_i)$, in which both structural and chemical data are taken into account. Several minimization cycles were performed until convergence was reached. Details on the minimization procedure are presented in Lavina et al. (2002). M-O and T-O bond distances were calculated as the linear

TABLE 1. Parameters for X-ray data collection

Determination of unit-cell parameters	
Radiation	Mo$K\alpha_1$ (0.70930 Å)
Reflections used	13 (Friedel pairs on both +2θ and −2θ)
Range	85–95° 2θ
Temperature	296 K
Diffraction intensity collection	
Radiation	Mo$K\alpha$ (0.71073 Å)
Monochromator	High-crystallinity graphite crystal
Range	3–95° 2θ
Reciprocal space range	$0 \le h \le 17; 0 \le k \le 17; 0 \le l \le 17$
Scan method	ω
Scan range	2.4°
Scan speed	Variable 1.502–14.648 °/min
Temperature	296 K
Data reduction	
Refinement	SHELXTL-PC
Corrections	Lorentz, Polarization
Absorption correction	Semi-empirical, 13 Ψ scans (10–95° 2θ)
Set of measured reflections	708–717
Set of unique reflections	147–149 [$I > 2\sigma(I)$]

TABLE 2. Results of the structural refinements

	MgMn01	MgMn05	MgMn10	MgMn20
a_0 (Å)	8.0883(3)	8.0965(5)	8.1321(6)	8.1413(4)
u	0.26213(4)	0.26212(7)	0.26232(6)	0.26231(6)
T-O (Å)	1.9211(3)	1.9229(6)	1.9342(5)	1.9362(5)
M-O (Å)	1.9290(3)	1.9310(5)	1.9380(5)	1.9403(4)
^{M}O-O$_{shared}$ (Å)	2.5822	2.5850	2.5917	2.5950
O-M-O (°)	84.03	84.03	83.93	83.93
m.a.n. T	12.33(7)	12.35(9)	13.73(9)	13.85(10)
m.a.n. M	13.01(4)	13.14(5)	14.11(4)	14.20(4)
U_{11} (T)	39(1)	42(3)	55(2)	59(2)
U_{11} (M)	41(1)	40(2)	53(1)	53(1)
U_{11} (O)	72(1)	81(2)	108(2)	107(1)
U_{12} (M)	−2(1)	−3(1)	−4(1)	−4(1)
U_{12} (O)	3(1)	0(1)	0(1)	−2(1)
Ext.	0.0041(1)	0.0039(2)	0.0053(1)	0.0053(1)
R (%)	1.48	2.24	1.64	1.83

Notes: m.a.n. = mean atomic number; U_{11} = displacement parameters (Å² × 10⁴); $U_{11} = U_{22} = U_{33}$ and $U_{12} = U_{13} = U_{23}$; Ext. = isotropic secondary extinction coefficient, according to Larson's algorithm (1970); R in the form: $(\Sigma|F_{obs} - F_{calc}|)/(\Sigma F_{obs})$. Space group $Fd\bar{3}m$, $Z = 8$.

contribution of each cation multiplied by its specific site bond distance, the latter refined on the basis of analysis of more than 250 spinel structural data from the literature (Lavina et al. 2002). However, the ionic radius for Mn³⁺ in tetrahedral coordination is not available from literature (e.g., see Shannon 1976). A bond distance of 1.88(1) Å for $^{IV}Mn^{3+}$ provided the best fits for the examined crystals. Final cation distributions, result of minimization calculations and $F(X_i)$ values are reported in Table 4.

Bond valence calculations

Experimental bond valences (S) were calculated on the basis of observed bond distances (R), by the formula $S = \exp[(R_0 - R)/0.37]$, where R_0 is an empirical parameter (Brown and Altermatt 1985). Furthermore, theoretical bond valences, s, (Brown 2002) for the M- and T-site, were calculated by the bond graph and the network equations related to the spinel topology. The bond distances associated with an unstrained spinel structure (R_{unstr}) have been calculated by the formula: $R_{unstr} = R_0 -0.37 \cdot \ln(s)$. In addition, the ideal geometrical parameters—a_{unstr}, u_{unstr}, $^M(O-O)_{shared-unstr}$, $O-M-O_{unstr}$—have been calculated using $T-O_{unstr}$ and $M-O_{unstr}$ (Table 5).

With respect to the unstrained spinel structure, the difference (Δv) between bond valence sums (BVS) and mean atomic valences $(<V>)$ at the T or M site indicates either overall overbonding or underbonding, which could lead to polyhedral compression or expansion, respectively. This is also reflected by the difference (Δd) between unstrained and observed bond distances for each polyhedron.

Optical absorption spectroscopy

Unpolarized optical absorption spectra in the UV/VIS range, 330–2000 nm (30 303 to 5000 cm⁻¹), were obtained at room temperature on double-sided polished single crystals mounted on glass slides. The crystals studied by optical absorption spectroscopy are identical to the ones we used for crystal structural refinements and EMP-analyses. The absorber thickness was in the range 20–112 μm as determined by means of a digital micrometer. Subsequent attempts to thin the absorbers further (<15 μm) were unsuccessful resulting in cracks and plucking. Spectra were recorded with a Zeiss MPM800 single beam microscope-spectrometer using Zeiss Ultrafluar 10× lenses as condenser and objective. In the UV/VIS-spectral range, a 75W Xenon arc lamp served as a light source and a photomultiplier as detector. In the NIR spectral region, 800–2000 nm (12 500–5000 cm⁻¹), a 100W halogen lamp was used as a light source and light detection was achieved by means of a photoconductive PbS-cell. Spectra were recorded at a spectral resolution of 2 nm in the UV/VIS range and 10 nm in the NIR region and the diameter of the measuring spot equaled 30 μm. Spectroscopic data were also obtained for the MIR range (10 000–2000 cm⁻¹) by means of an FTIR spectrometer (Bruker Equinox 55S) equipped with an IR microscope. These spectra were recorded at a resolution of 8 cm⁻¹ with measuring areas around 75 × 75 μm using a tungsten lamp as source, CaF₂ beam splitter, and an MCT detector. Fits of the recorded spectra were carried with the Jandel PeakFit software under the assumption of Gaussian peak shapes.

TABLE 3. Chemical composition (EMPA) of the studied spinel single crystals

	MgMn01	MgMn05	MgMn10	MgMn20
Al₂O₃ (wt%)	71.1(2)	69.5(4)	60(2)	58.4(5)
MgO	28.1(2)	26.9(2)	23.5(6)	23.7(1)
MnO	0.65(9)	2.9(4)	15(2)	16.6(7)
MnO*	0.26	1.61	5.24	4.81
Mn₂O₃*	0.43	1.39	11.06	13.11
Cations on basis of 4 O atoms				
Al	1.992(5)	1.974(9)	1.79(4)	1.75(1)
Mg	0.995(4)	0.967(7)	0.89(3)	0.897(8)
Mn²⁺	0.005(2)	0.033(8)	0.11(4)	0.10(1)
Mn³⁺	0.008(4)	0.026(8)	0.21(3)	0.25(1)
epfu chemical†	38.2	38.7	42.0	42.4
epfu SREF‡	38.3(1)	38.6(1)	42.0(1)	42.3(1)

Notes: Digits in brackets = standard deviation (1σ) for both oxides and cations; epfu = electrons per formula unit.
* From stoichiometry.
† Sum of scattering (epfu) of cation populations derived from chemical analysis.
‡ Sum of refined site-scattering (epfu) derived from SREF.

Single crystals

The synthesized crystals, which represent the Mg-rich part of the MgAl₂O₄-MgMn₂O₄ solid solution, have a pseudo-octahedral shape and range in size from 100 to 300 μm. Their color changes from faint yellow over yellowish brown and reddish brown with increasing Mn content (Fig. 1).
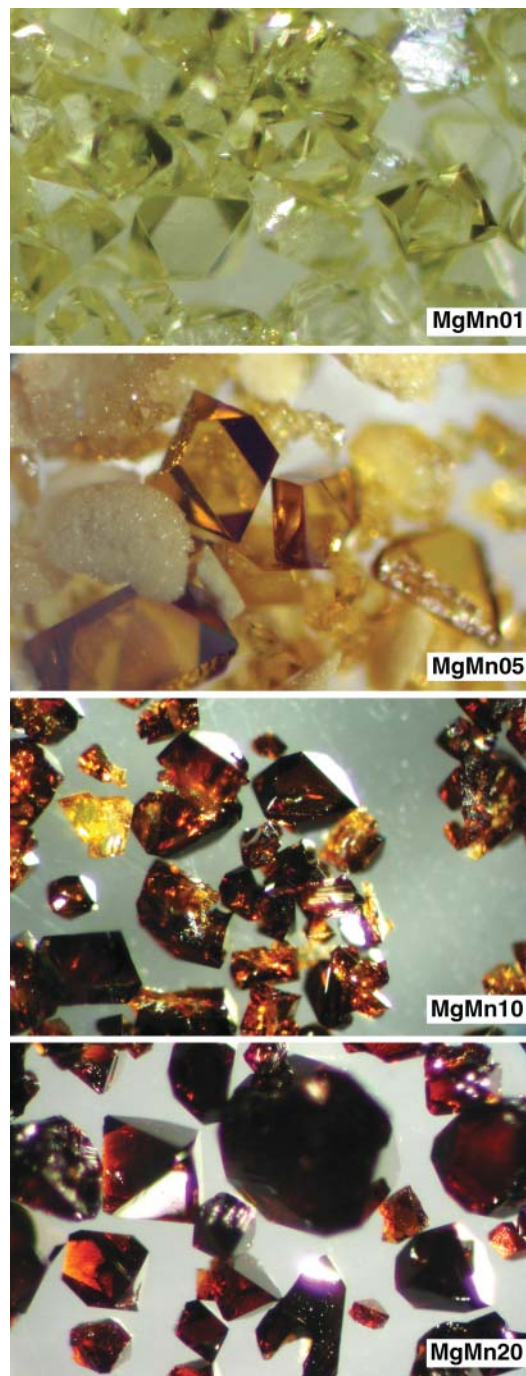

FIGURE 1. Microphotographs of Mn-doped spinels showing from top to bottom the color changes with increasing Mn-content.

Chemical composition and structural parameters

In general, the crystals were found to be chemically homogeneous, but some of the most Mn-rich crystals, especially those from MgMn10 synthesis run, exhibit variable degrees of chemical zoning with an increase in Mn-content and an antipathetic decrease in Al-content from core to rim (Fig. 2). Obviously, these highly zoned crystals were not suitable for the following single-crystal structural refinement (SREF) analysis, and the more homogeneous crystals within each run were selected for the structural study. In spite of this, the selected MgMn10 crystal still shows some inhomogeneity (reflected by high standard deviations of mean chemical data).

Crystal compositions are characterized by Mn³⁺-contents progressively increasing up to 0.25 atoms per formula unit (apfu), paralleled by a decrease of Al-contents from 1.99 to 1.75 apfu. Moreover, some Mn²⁺ was found, which increases up to 0.11 apfu with total Mn, paralleled by an Mg decrease from 1.00 to 0.90 apfu (Table 3). Consequently, the main exchange is the homovalent substitution $Mn^{3+} \rightarrow Al$.

The unit-cell parameter increases from 8.0883(3) to 8.1413(4) Å and is principally related to the increasing Mn³⁺ content, as revealed by the following relationship: $a_0 = 8.0889 + 0.2056\, Mn^{3+}$ apfu ($r^2 = 0.995$). The u parameter increases from 0.26212(7) to 0.26232(6) and is more correlated with total Mn content.

Cation distribution

The investigated Mn-doped spinels show a complex distribution of Mg, Mn²⁺, Mn³⁺, and Al. The sum of total site scattering derived by chemical analysis and that obtained by SREF are in agreement (Table 3) and consistent with spinel stoichiometry, which indicates that cation vacancies are insignificant in our crystals. Different distribution trends are observed along the present restricted part of the MgAl₂O₄–MgMn₂O₄ join, highlighting some interesting crystal-chemical features (Table 4). The Mg population in the T site remains constant, while Mg in the M site decreases through replacement by Mn²⁺. Similarly, the Al
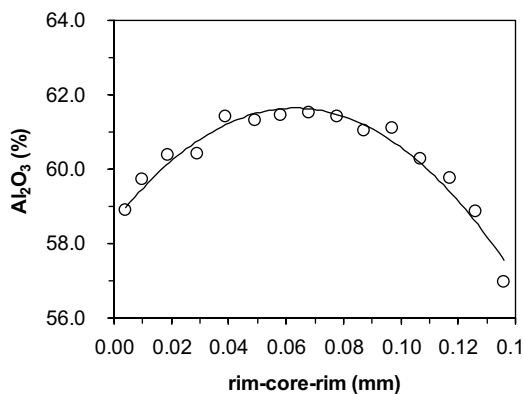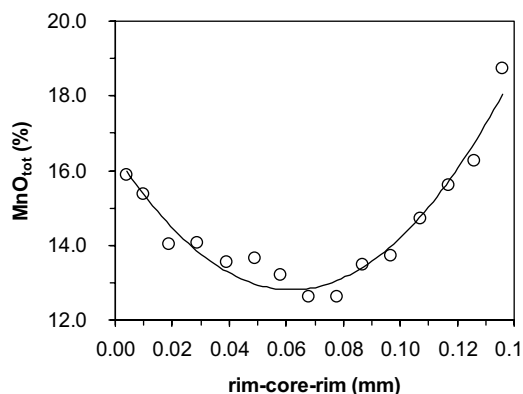
TABLE 4. Final assigned site populations (apfu) and differences between observed and calculated structural and chemical parameters from minimization procedure

	MgMn01	MgMn05	MgMn10	MgMn20
T site				
Al	0.234(2)	0.228(3)	0.134(11)	0.104(3)
Mg	0.760(4)	0.757(6)	0.749(25)	0.758(7)
Mn²⁺	0.003(2)	0.013(5)	0.027(21)	0.013(5)
Mn³⁺	0.003(1)	0.003(1)	0.089(25)	0.126(8)
ΣT	1.000	1.000	1.000	1.000
M site				
Al	1.758(4)	1.744(8)	1.674(38)	1.646(11)
Mg	0.234(2)	0.209(3)	0.138(11)	0.141(3)
Mn²⁺	0.003(1)	0.022(6)	0.085(39)	0.088(13)
Mn³⁺	0.006(4)	0.025(7)	0.103(27)	0.124(8)
ΣM	2.000	2.000	2.000	2.000
F(Xi)	0.39	0.17	0.40	0.05
Δa (Å)	0.0000	0.0001	0.0005	0.0000
Δu	0.00000	0.00001	0.00000	0.00001
ΔT-O (Å)	0.0000	0.0001	0.0001	0.0000
ΔM-O (Å)	0.0000	0.0001	0.0001	0.0000
Δ T m.a.n.	0.01	0.08	0.08	0.05
Δ M m.a.n.	0.08	0.04	0.05	0.00
ΔAl (apfu)	0.001	0.002	0.021	0.003
ΔMg (apfu)	0.001	0.002	0.000	0.003
ΔMn²⁺ (apfu)	0.001	0.002	0.000	0.003
ΔMn³⁺ (apfu)	0.001	0.002	0.021	0.003

Notes: F(Xi) = sum of square residuals divided by number of observed parameters; Δ = (observed – calculated) absolute differences.

TABLE 5. Bond valences and ideal parameters

	MgMn01	MgMn05	MgMn10	MgMn20
S_{T-O} (v.u.)	0.526	0.526	0.525	0.526
S_{M-O} (v.u.)	0.479	0.479	0.479	0.478
BVS_T (v.u.)	2.106	2.102	2.101	2.103
BVS_M (v.u.)	2.872	2.871	2.872	2.865
$<V>_T$ (v.u.)	2.237	2.231	2.224	2.230
$<V>_M$ (v.u.)	2.882	2.885	2.888	2.885
GII (v.u.)	0.06	0.06	0.06	0.06
Δv_T (v.u.)	−0.131	−0.128	−0.123	−0.127
Δv_M (v.u.)	−0.010	−0.014	−0.016	−0.020
s_{T-O} (v.u.)	0.559	0.558	0.556	0.557
s_{M-O} (v.u.)	0.480	0.481	0.481	0.481
$a_{0\,unstr}$ (Å)	8.0529	8.0602	8.0963	8.1032
u_{unstr}	0.26113	0.26117	0.26143	0.26141
T-O$_{unstr}$ (Å)	1.8987	1.9010	1.9132	1.9145
M-O$_{unstr}$ (Å)	1.9278	1.9292	1.9359	1.9378
ᴹO-O$_{shared-unstr}$ (Å)	2.5936	2.5951	2.6007	2.6035
O-M-O$_{unstr}$ (°)	84.55	84.53	84.39	84.41
Δd_T (Å)	−0.0224	−0.0219	−0.0210	−0.0217
Δd_M (Å)	−0.0012	−0.0018	−0.0021	−0.0025

Notes: S = experimental bond valence, BVS = bond valence sum, $<V>$ = mean atomic valence, GII = global instability index, Δv = BVS − $<V>$, s = theoretical bond valence, Δd = (unstrained bond distance) – (observed bond distance).

FIGURE 2. Chemical zoning of the MgMn10 crystal: analyses along N-S alignment (15 points, step 10 μm). Symbol size is larger than experimental analytical error.

population in the T site decreases, through substitution by Mn^{3+}. Exactly the same applies for the M site. As a consequence, the inversion parameter is almost constant at $i = 0.23(1)$, which is a value closely comparable to the inversion degree observed in $MgAl_2O_4$ equilibrated at ca. 800 °C (Andreozzi and Princivalle 2002).

In the Mn-richest samples, Mn^{3+} is distributed over both sites, but the occupancy of the T site is double compared to that of the M site. Also Mn^{2+} is distributed over both sites, but with prevalence for the M-site. This is completely different from what observed in galaxite ($Mn^{2+}Al_2O_4$), where Mn^{2+} was strongly ordered at the T site (Lucchesi et al. 1997). Consequently, a disordered distribution of Mn^{2+} and Mn^{3+} was observed in our samples, which is quite surprising, but is also reflected by m.a.n. values greater than 13.00 in both T and M sites at high Mn_{tot}. Although Mn^{3+} may be present in the M- as well as T-sites in the tetragonal spinelloid phase $MgMn_2O_4$ (Keer et al. 1974; Radhakrishnan and Biswas 1975, 1976; Malavasi et al. 2002, 2005), no evidence for a comparable disorder in cubic spinel has been reported so far.

Optical absorption spectroscopy

The recorded spectra show broad absorption features at ca. 23 000 and 10 800 cm^{-1} (Fig. 3). The absorption feature at 23 000 cm^{-1} is highly skewed and fits of the recorded spectra strongly suggest that this feature consists of two relatively broad and partly overlapping absorption bands at 23 600 and 21 200 cm^{-1}, on which narrow and relatively weak bands at 23 300, 22 100 and 21 000, 19 900, and 18 000 cm^{-1} are superimposed. The intensity of this high-energy absorption increases systematically with increasing Mn-content. The absorption band at ca. 10 800 cm^{-1} is very weak in the two samples with the lowest Mn-contents, but it becomes a prominent feature in spectra of the more Mn-rich samples (Fig. 3). The intensity of the UV-absorption edge, which is caused by ligand-metal charge transfer processes, increases strongly with the Mn-content of the samples and causes a pro-

nounced shift of the edge absorption into the visible spectral range. This precluded spectral recording of the absorption feature at 23 000 cm^{-1} in the two most Mn-rich samples, even when strongly thinned (<15 μm).

DISCUSSION

Crystal chemistry

The results of the bond valence approach to the Mn-doped spinels show the presence of lattice-induced strain (Table 5). In fact, all the crystals have a Global Instability Index (GII), as defined by Brown (2002), equal to 0.06 valence units (v.u.), which indicates strained bonds. In particular, the bonds are stretched in the tetrahedron (Δv_T and Δd_T negative) indicating underbonding in T, whereas the bonds are unstrained in the octahedron (Δv_M and Δd_M close to zero). This steric effect is associated with the cations at the T-site, which are too small compared to the ideal size and lead to Δd_T values of about –0.022 Å (Table 5). To reduce the M-M repulsion, the steric effect is driven by the movement of the oxygen atoms, which improves the shielding effect around the M-site, thus increasing the distortion of the structure relative to the CCP. The comparison between ideal and real structure (Tables 2 and 5) shows that the oxygen array is less distorted at unstrained conditions than at strained ones, $u_{unstr} < u_{obs}$, and consequently also the octahedron is more regular, $(O-M-O)_{unstr} > (O-M-O)_{obs}$. To retain structural stability, the oxygen array distorts (u increases) and the T-O bonds lengthen. In accordance with the distortion theorem (Brown 2002), the symmetry of the T-site does not allow extensive bond relaxation. As a consequence, the bond valence sum around the T-site differs from the expected mean atomic valence and the tetrahedron undergoes an isotropic expansion. This expansion (Δd_T = –0.022 Å) is consistent with the longer $^{IV}Mn^{3+}$-O bond distance here refined [1.88(1) Å] with respect to that calculated on the basis of the bond-valence constant and coordination number related to $^{IV}Mn^{3+}$: i.e., $1.760 – 0.37 \cdot \ln(3/4) = 1.866$ Å.

Assignments of optical absorption bands

The absorption bands at 23 600, 21 200, and 10 800 cm^{-1} reveal features (absorption coefficients and band widths) in accordance with spin-allowed electronic transitions in 3d-cations. The only 3d-cation in which such transitions may occur in the present synthetic samples is Mn^{3+}. Two different main assignment models may be considered for these bands. One involves transitions in octahedrally coordinated Mn^{3+} exclusively, while an alternative model relates to spin-allowed d-d transitions in octahedrally as well as tetrahedrally coordinated Mn^{3+}. The very low relative intensity of the absorption band at 10 800 cm^{-1} in the spectra of the two samples with the lowest Mn^{3+}-contents suggests that this band is caused by electronic processes in cations in a different environment than those giving rise to the high-energy bands. Consequently, we prefer the alternative model, which is also consistent with the cation distribution determined from our single-crystal structure refinements.

This assignment model would require that the symmetry of the M- and T-sites in the present spinels is close to the ideal O_h and T_d. Within this framework, the absorption feature at ca. 23 000 cm^{-1} is assigned to the spin-allowed $^5E_g \rightarrow ^5T_{2g}$ transition in octahedrally coordinated Mn^{3+}. The observed splitting of the
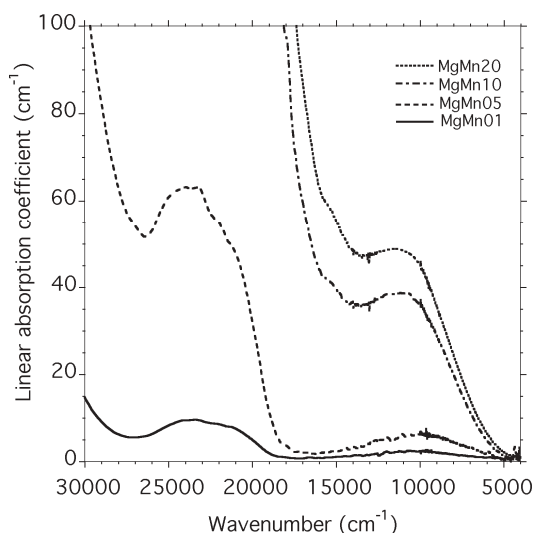

FIGURE 3. Unpolarized optical absorption spectra of Mn-doped spinel single crystals.

absorption band into two components at 23 600 and 21 200 cm^{-1} may be related to a dynamic Jahn-Teller effect, which produces transient splitting of t_{2g}-orbitals in Mn^{3+}. Alternatively, the splitting may be caused by structural relaxations leading to local deviations from O_h-symmetry of the Mn^{3+}-centered M-sites. However, the results of our structural refinements suggest that the M-site may only be subject to minor local deviations from O_h-symmetry. The remaining strong absorption band at ca. 10 800 cm^{-1} is assigned to the $^5T_{2g} \rightarrow {}^5E_g$ transition in tetrahedrally coordinated Mn^{3+}. Based on the above assignments, the crystal field splitting, 10Dq (Δ), for Mn^{3+} at the octahedral M- and tetrahedral T-site is calculated to be 22 400 and 10 800 cm^{-1}, respectively. This results in a Δ_t/Δ_o-ratio of ca. 0.48 for Mn^{3+} in the spinel structure, which is in very good agreement with the expected value of 0.44 (e.g., Burns 1993).

The Δ_o-value for Mn^{3+} in the present spinels is considerably higher than those determined for Mn^{3+} at octahedral sites in several silicates. For instance, Δ_o-values in the range 13 500–15 500 cm^{-1} have been recorded for Mn^{3+} in the highly distorted MO_6-octahedra in piemontite and kanonaite (e.g., Abs-Wurmbach et al. 1981; Smith et al. 1982). The higher Δ_o-value for Mn^{3+} in spinel is related to the considerably shorter octahedral mean M-O distances in our spinel samples (1.93–1.94 Å) as compared to the mean octahedral M-O distances of 2.062 and 2.022 Å in piemontite (Dollase 1969) and kanonaite (Schreyer et al. 2004), respectively.

The tetrahedral coordination of the Mn³⁺

The high space group symmetry of spinel does not allow bond distance distortions and thus the structure behaves rigidly. Simultaneously, the spinel group is characterized by a considerable chemical flexibility. This apparent contradiction is explained by an optimal cation partition related to cation radii, which compensates for the intrinsic structural rigidity. The importance of steric factors for the cation distribution is exemplified by, e.g., $FeAl_2O_4$, $CoAl_2O_4$, and $CuAl_2O_4$ spinels (Harrison et al. 1998; O'Neill 1994; O'Neill et al. 2005), in which the small Al cation orders in the larger octahedra. In these spinels, cation size and crystal field stabilization energy (CFSE) suggest that Co^{2+}, Fe^{2+}, and Cu^{2+} should prefer the M-sites, but the presence of Al obviously counteracts this behavior. Similarly, in our crystals, Mn^{3+} is expected to order at the M-site on the basis of size and CFSE arguments, but because of the ability for tetrahedral expansion the structure preferentially incorporates larger cations such as Mn^{3+} ($^{IV}Mn^{3+}$-O = 1.88 Å) rather than smaller cations like Al (^{IV}Al-O =1.774 Å) at the T-site.

A comparable illustration of the importance of steric factors on the cation distribution in the spinel structure is magnesioferrite, $MgFe_2O_4$, in which $^{IV}Fe^{3+}$-O = 1.875 Å (Lavina et al. 2002) is very close to the observed $^{IV}Mn^{3+}$-O bond length in our samples. Experimental data on the Fe^{3+} site distribution in spinels in the system $MgAl_{2-x}Fe_xO_4$ (Andreozzi et al. 2001; Nakatsuka et al. 2004; Martignago et al. 2006) show large similarities with the Mn^{3+} site distribution in the present Mn-doped spinels (Fig. 4). This is consistent with the very similar cation radii observed for high spin Fe^{3+} and Mn^{3+}, but does not reflect the large difference in CFSE and consequently also in octahedral site preference energy for Fe^{3+} and Mn^{3+} (0 and –95.4 kJ/mol, respectively;
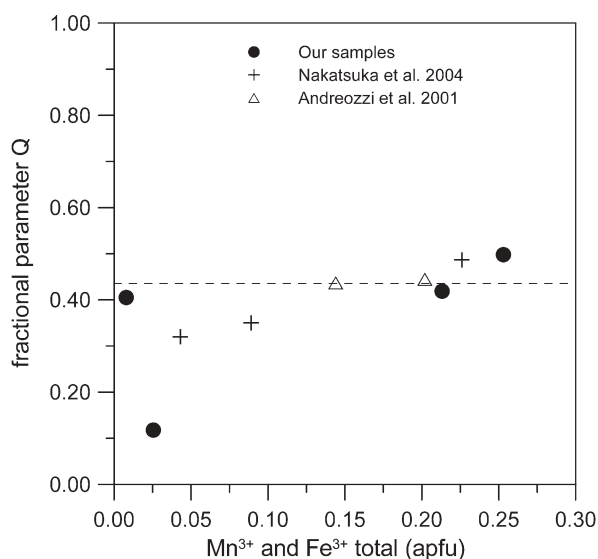
FIGURE 4. Fractional parameters Q_{Mn3+} ($^TMn^{3+}/Mn^{3+}_{tot}$) and Q_{Fe3+} ($^TFe^{3+}/Fe^{3+}_{tot}$) vs. Mn^{3+} and Fe^{3+} concentration, respectively. The fractional parameter estimates the site selectivity of the cations. *Dashed-dotted line* at Q = 0.44 represents the value of Q_{Fe3+} in the $MgAl_2O_4$-$MgFe_2O_4$ series observed by Nakatsuka et al. (2004).

Burns 1993). These values would suggest large differences in cation distribution and therefore the observed similarities are surprising. Obviously, the importance of the CFSE-term is a less important factor than generally believed. This conclusion is also supported by computational studies (Della Giusta and Ottonello 1993), which indicate that the importance of the CFSE is largely overestimated and that coulombic and repulsive terms are by far the most important terms for intracrystalline disorder in spinels.

REFERENCES CITED

Abs-Wurmbach, I., Langer, K., Seifert, F., and Tillmanns, E. (1981) The crystal chemistry of (Mn^{3+}, Fe^{3+})-substituted andalusites (viridines and kanonaite), ($Al_{1-x-y}Mn_x^{3+}Fe_y^{3+}$)$_2$(O|SiO$_4$): crystal structure refinements, Mössbauer, and polarized optical absorption spectra. Zeitschrift für Kristallographie, 155, 81–113.

Andreozzi, G.B. and Princivalle, F. (2002) Kinetics of cation ordering in synthetic $MgAl_2O_4$ spinel. American Mineralogist, 87, 838–844.

Andreozzi, G.B., Hålenius, U., and Skogby H. (2001) Spectroscopic active $^{IV}Fe^{3+}$-$^{VI}Fe^{3+}$ clusters in spinel-magnesioferrite solid solution crystals: a potential monitor for ordering in oxide spinels. Physics and Chemistry of Minerals, 28, 435–444.

Bosi, F., Andreozzi, G.B., Ferrini, V., and Lucchesi, S. (2004) Behavior of cation vacancy in kenotetrahedral Cr-spinels from Albanian eastern belt ophiolites. American Mineralogist, 89, 1367–1373.

Brown, I.D. (2002) The chemical bond in inorganic chemistry: the bond valence model, 12, 288 p. International Union of Crystallography Monographs on Crystallography, Oxford University Press, U.K.

Brown, I.D. and Altermatt, D. (1985) Bond-valence parameters obtained from a systematic analysis of the Inorganic Crystal Structure Database. Acta Crystal-

lographica, B41, 244–247.

Burns, R.G. (1993) Mineralogical Applications of Crystal Field Theory (2nd edition), 551 p. Cambridge Univeristy Press, U.K.

Della Giusta, A. and Ottonello, G. (1993) Energy and long-range disorder in simple spinels. Physics and Chemistry of Minerals, 20, 228–241.

Della Giusta, A., Carbonin, S., and Ottonello, G. (1996) Temperature-dependent disorder in a natural Mg-Al-Fe^{2+}-Fe^{3+}-spinel. Mineralogical Magazine, 60, 603–616.

Dollase, W.A. (1969) Crystal structure and cation ordering of piemontite. American Mineralogist, 54, 710–717.

Golikov, Y.V., Barkhatov, V.P., Balakirev, V.F., and Avdukov, V.I. (1989) High-temperature and quenched states in manganese-containing oxide systems in air. High Temperatures-High Pressures, 21, 685–700.

Harrison, R.J., Redfern, S.A.T., and O'Neill, H.St.C. (1998) The temperature dependence of the cation distribution in synthetic hercynite (FeAl$_2$O$_4$) from in-situ neutron structure refinements. American Mineralogist, 83, 1092–1099.

Hill, R.J., Craig, J.R., and Gibbs, G.V. (1979) Systematics of the spinel structure type. Physics and Chemistry of Minerals, 4, 317–340.

Keer, H.V., Bodas, M.G., Bhaduri, A., and Biswas, A.B. (1974) Electrical and magnetic properties of the MgMn$_2$O$_4$–MgAl$_2$O$_4$ system. Journal of Physics D: Applied Physics, 7, 2058–2062.

Larson, A.C. (1970) Crystallographic Computing, F.R. Ahmed, S.R. Hall, and C.P. Huber, Eds., p. 291–294. Munksgaard, Copenhagen.

Lavina, B., Salviulo, G., and Della Giusta, A. (2002) Cation distribution and structure modeling of spinel solid solutions. Physics and Chemistry of Minerals, 29, 10–18.

Lavina, B., Reznitskii, L.Z., and Bosi, F. (2003) Crystal chemistry of some Mg, Cr, V normal spinels from Sludyanka (Lake Baikal, Russia): the influence of V^{3+} on structural stability. Physics and Chemistry of Minerals, 30, 599–605.

Lucchesi, S., Russo, U., and Della Giusta, A. (1997) Crystal chemistry and cation distribution in some Mn-rich natural and synthetic spinels. European Journal of Mineralogy, 9, 31–42.

Malavasi, L., Ghigna, P., Chiodelli, G., Maggi, G., and Flor, G. (2002) Structural and transport properties of Mg$_{1–x}$Mn$_x$Mn$_2$O$_{4\pm\delta}$ spinels. Journal of Solid State Chemistry, 166, 171–176.

Malavasi, L., Tealdi, C., Amboage, M., Mozzati, M.C., and Flor, G. (2005) High-pressure X-ray diffraction study of MgMn$_2$O$_4$ tetragonal spinel. Nuclear Instruments and Methods in Physics Research B, 238, 171–174.

Martignago, F., Andreozzi, G.B., and Dal Negro, A. (2006) Thermodynamics and kinetics of cation ordering in natural and synthetic Mg(Al, Fe^{3+})$_2$O$_4$ spinels

from in situ high-temperature X-ray diffraction. American Mineralogist, 91, 306–312.

Matsubara, S., Kato, A., and Nagashima, K. (1979) Iwakiite, Mn^{2+}(Fe^{3+}, Mn^{3+})$_2$O$_4$, a new tetragonal spinelloid mineral from the Gozaisho mine, Fukushima Prefecture, Japan. Mineralogical Journal, 9, 383–391.

Nakatsuka, A., Ueno, H., Nakayama, N., Mizota, T., and Maekawa, H. (2004) Single-crystal X-ray diffraction study of cation distribution in MgAl$_2$O$_4$–MgFe$_2$O$_4$ spinel solid solution. Physics and Chemistry of Minerals, 31, 278–287.

North, A.C.T., Phillips, D.C., and Mathews, F.S. (1968) A semi-empirical method of absorption correction. Acta Crystallographica, A24, 351–359.

O'Neill, H.St.C. (1994) Temperature dependence of the cation distribution in CoAl$_2$O$_4$ spinel. European Journal of Mineralogy, 6, 603–609.

O'Neill, H.St.C., James, M., Dollase, W.A., and Redfern, S.A.T. (2005) Temperature dependence of the cation distribution in CuAl$_2$O$_4$ spinel. European Journal of Mineralogy, 17, 581–586.

Pouchou, J.L. and Pichoir, F. (1984) A new model for quantitative X-ray microanalysis. I. Application to the analysis of homogeneous samples. La Recherche Aérospatiale, 3, 13–36.

Radhakrishnan, N.K. and Biswas A.B. (1975) Cation distribution in the tetragonal spinel MgMn$_2$O$_4$. Zeitschrift für Kristallographie, 142, 121–126.

——— (1976) A neutron diffraction study of the cation migration in MgMn$_2$O$_4$. Physical Status Solid, 37A, 719- 722.

Schreyer, W., Bernhardt, H.J., Fransolet A.M., and Armbruster, T. (2004) End-member ferrian kanonaite: an andalusite phase with one Al fully replaced by (Mn, Fe)$^{3+}$ in a quartz vein from the Ardennes mountains, Belgium, and its origin. Contributions to Mineralogy and Petrology, 147, 276–287.

Shannon, R.D. (1976) Revised Effective Ionic Radii and Systematic Studies of Interatomic Distances in Halides and Chalcogenides. Acta Crystallographica, A32, 751–767.

Smith, G., Hålenius, U., and Langer, K. (1982) Low-temperature spectral studies of Mn^{3+}-bearing andalusite and epidote type minerals in the range 30000–5000 cm^{-1}. Physics and Chemistry of Minerals, 8, 136–142.

Tokonami, M. and Horiuchi, H. (1980) On the space group of spinel MgAl$_2$O$_4$. Acta Crystallographica, A36, 122–126.